

Supporting Information for

Highly Active Single-Layer MoS₂ Catalyst Synthesized by Swift Heavy Ion Irradiation

Lukas Madau^{1‡}, Ioannis Zegkinoglou^{2‡}, Henrique Vázquez Muiños³, Yong-Wook Choi², Sebastian Kunze², Meng-Qiang Zhao⁴, Carl H. Naylor⁴, Philipp Ernst¹, Erik Pollmann¹, Oliver Ochedowski¹, Henning Lebius⁵, Abdenacer Benyagoub⁵, Brigitte Ban-d'Etat⁵, A. T. Charlie Johnson⁴, Flyura Djurabekova³, Beatriz Roldan Cuenya,^{2,6*} and Marika Schleberger^{1*}

1. Faculty of Physics and CENIDE, Universität Duisburg-Essen, 47057 Duisburg, Germany
2. Department of Physics, Ruhr-Universität Bochum, 44780 Bochum, Germany
3. Department of Physics, University of Helsinki, P.O. Box 43, 00014, Helsinki, Finland
4. Department of Physics and Astronomy, University of Pennsylvania, Philadelphia, USA
5. CIMAP, (CEA-CNRS-ENSICAEN-UCN), blvd Henri Becquerel, Caen, France
6. Department of Interface Science, Fritz-Haber Institute of the Max Planck Society, Berlin, Germany

* Corresponding author: marika.schleberger@uni-due.de

roldan@fhi-berlin.mpg.de

MoS₂ growth:

Monolayer MoS₂ flakes were grown directly on a 300 nm SiO₂/Si substrate by CVD. First, a 1% sodium cholate solution, known to act as a growth promoter for MoS₂, is spin-coated at 4000 rpm for 60 s onto the SiO₂ substrate. A droplet of a saturated solution of ammonium heptamolybdate in deionized (DI) water is deposited onto the substrate, providing the molybdenum feedstock. The substrate is placed in the center of a 1 in. CVD tube furnace and 15 mg of solid sulphur is placed 15 cm upstream from the substrate. Growth occurs at an atmospheric pressure in a flow of 750 sccm of nitrogen gas (99.999% purity). The furnace temperature is ramped to 750 °C at a rate of 70 °C min⁻¹. While the Mo source and SiO₂ growth substrate reach 750 °C, the maximum temperature of the sulphur is ~150 °C. After a 15 min growth period, the furnace is opened, and the sample is rapidly cooled to room temperature in 1000 sccm flowing nitrogen.

MoS₂ transfer:

The transfer of MoS₂ to the GC substrates was accomplished by spin-coating PMMA onto the as-grown sample, which was then placed in a bath of 0.1 M KOH to slowly etch the SiO₂ surface and release the PMMA/MoS₂ layer from the substrate. The floating PMMA/MoS₂ layer was then transferred into successive water baths for cleaning and finally scooped onto a target substrate. The sample was then dried, and the PMMA was removed with an acetone spray, followed by an acetone bath.

Ion irradiation:

Swift Heavy Ion (SHI) irradiation was performed at the IRRSUD beamline of the GANIL facility in Caen, France. ¹²⁹Xe⁺²³ ions with a kinetic energy of 0.71 MeV/u were used. The calibration of the angle of incidence was performed as follows: First, a telescope was mounted on the optical axis of the beamline. The position at which the surface of the sample is parallel to the optical axis was determined as zero degrees. Second, a SrTiO₃ sample was irradiated under a non-zero angle with a fixed fluence (ions/μm²). Analysis with AFM afterwards allows us to determine the density of ion impacts on the SrTiO₃ surface (defect creation efficiency of SHI in SrTiO₃ is one). As the density of ion impacts scales with sinθ (in which θ is the angle of incidence with respect to the surface), we can compare the experimentally determined angle of incidence with the chosen one and calibrate the setup.

Raman- and photoluminescence analysis:

Fig. S1 compares Raman- and photoluminescence (PL) measurements of SHI irradiated CVD grown single-layer MoS₂. The results are presented as a single point measurement in S1 (a) and as mappings in S1 (b)-(e). Fig. S1 (a) gives an impression of the crystallinity of the MoS₂ flakes prior and after irradiation taking the amount of photoluminescence of the MoS₂ after laser excitation as a measure for the degree of crystallinity. Comparing the intensity of the typical Raman active A_{1g} and E_{2g}¹ in MoS₂ (~ 385 cm⁻¹ and 404 cm⁻¹) with the PL peak (~ 3900 cm⁻¹) the MoS₂ shows high crystallinity prior to irradiation (black curve). After irradiation one can still clearly observe both the Raman modes as well as a PL peak, however, due to ion irradiation and defect creation, the crystallinity of the MoS₂ has obviously degraded.

Fig. S1 (b)-(c) presents PL mappings of non-irradiated (b) and irradiated (c) MoS₂. As expected, non-irradiated MoS₂ shows a homogeneous PL over the whole sample. Irradiated MoS₂ in contrast shows a rather inhomogeneous PL signal over the MoS₂ samples, which can be attributed to the ripping and tearing of the MoS₂ caused by ion impact, as shown in the SEM in the manuscript in Fig. 2. A similar

behavior can be observed when analyzing the distance of the Raman active A_{1g} and E_{2g}^1 modes in Fig. S1 (d)-(e). Pristine MoS_2 in Fig. S1 (d) shows a Raman mode difference of $\sim 21 \text{ cm}^{-1}$ evenly distributed over the sample. Irradiated MoS_2 however, shows a varying mode difference. It has been shown that a varying distance of the A_{1g} and E_{2g}^1 mode can be explained by a locally varying degree of strain and/or doping in the MoS_2 .^{1,2} Considering the 3D Origami-like foldings of the MoS_2 (see Fig. 2 in manuscript) SHI impacts under grazing incidence are likely to induce also strain in the MoS_2 , aside from foldings and incisions. Also, due to the adsorption of oxygen at the under-coordinated Mo edges, it is likely that the MoS_2 will experience a p-doping, which also causes an increase in the distance of the Raman modes.^{3,4}

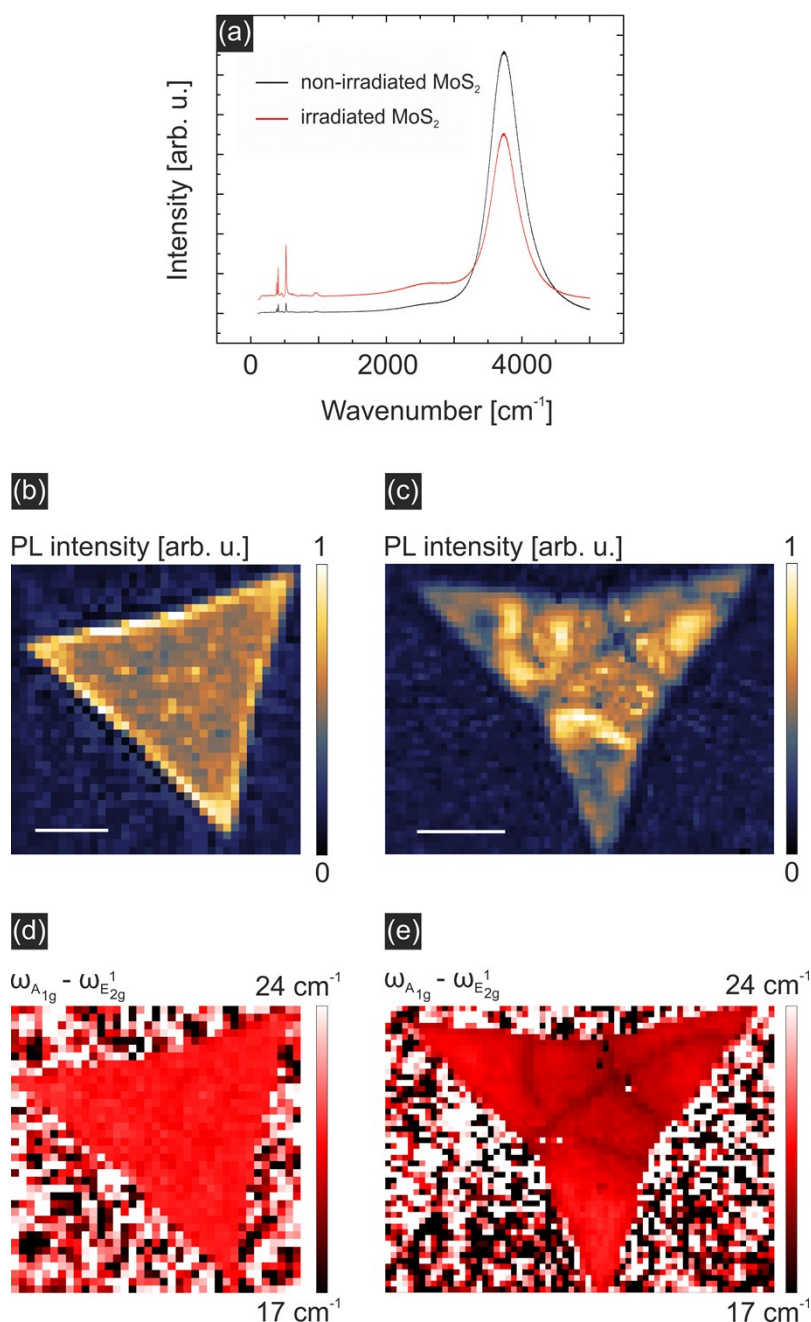


Figure S1: (a) Point measurement of non-irradiated (black curve) and irradiated (red curve) showing MoS_2 Raman active modes and PL peak. Mappings of PL peak intensity of non-irradiated (b) and irradiated MoS_2 (c). The intensity of the PL mappings is each normalized. Mapping of the distance of

the Raman active A_{1g} and E_{2g}^1 modes of pristine (d) and irradiated MoS_2 (e). Measurements were performed with a 532 nm laser. Ion fluence for the irradiated samples was chosen to 2300 ions/ μm^2 .

SEM analysis:

SEM images of irradiated (Fig. S2 (a)) and non-irradiated (Fig. S2 (b)) MoS_2 /glassy carbon surfaces demonstrate the morphological changes induced by SHI irradiation. While the pristine MoS_2 on glassy carbon shows no structural irregularities, one can clearly observe incisions in the MoS_2 both on SiO_2 (Fig. 2 in manuscript) and on glassy carbon (Fig. 2 (d) in manuscript and Fig. S2 (a)) substrates after ion irradiation.

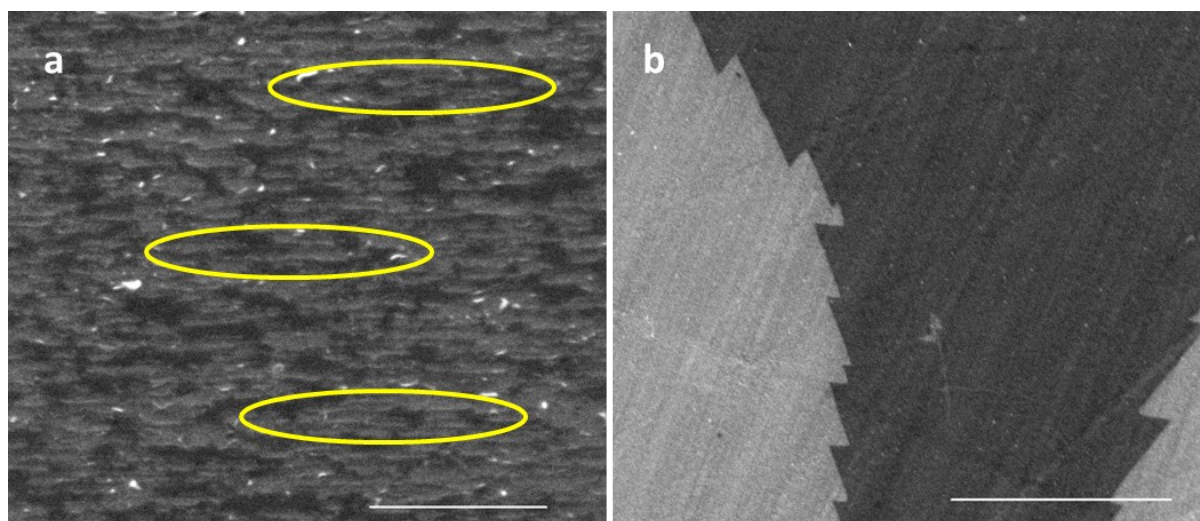


Figure S2. SEM images of (a) ion-irradiated MoS_2 on glassy carbon, and (b) of a non-irradiated, nominally identical sample. The irradiation-induced incisions are visible in (a) (elongated features extending from left to right, examples shown in ovals). The length scale in (a) corresponds to 2 μm (magnification factor 20000), in (b) to 5 μm (magnification factor 10000).

Fig. S3 presents additional SEM images of irradiated (a) and non-irradiated (b) MoS_2 /glassy carbon samples. The 3D structures (white details in circles) are only present in the irradiated samples and moreover only in the MoS_2 covered part. Bare glassy carbon areas (lower right part in (a)) show no such structures. Non-irradiated samples (Fig. S3 (b)) show no such features, neither on the MoS_2 covered parts nor on the glassy carbon parts.

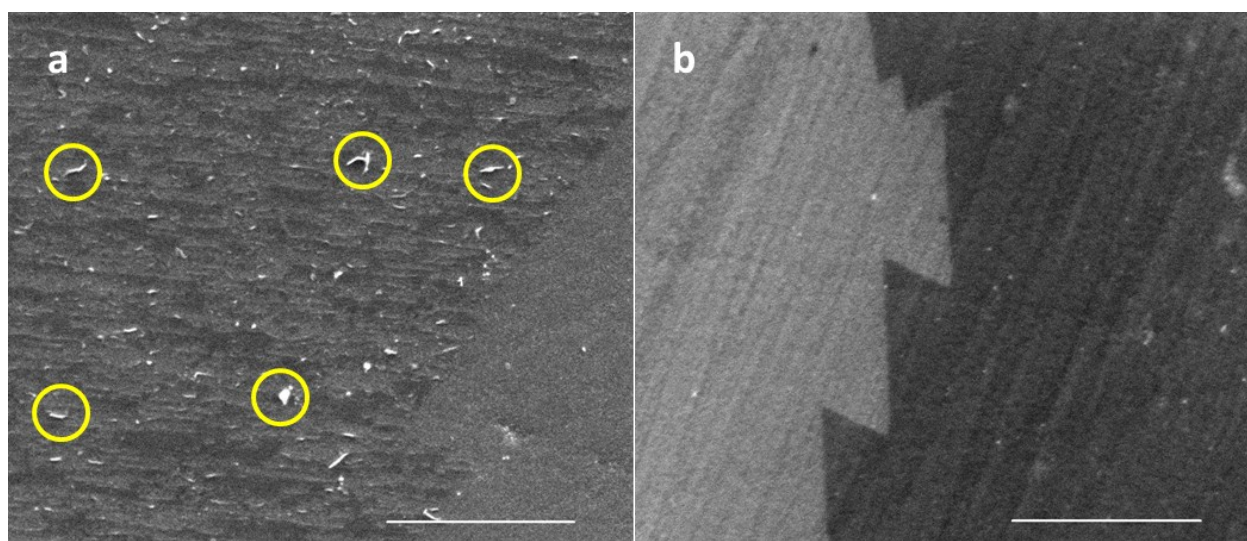


Figure S3. SEM images of (a) ion-irradiated MoS₂ on glassy carbon, and (b) of a non-irradiated, nominally identical sample. The 3D structures are clearly visible on the MoS₂ covered part of the sample in (a), with examples highlighted within circles. The glassy carbon substrate (lower right part of (a)) is not significantly affected by the irradiation and exhibits no 3D structures. The length scale corresponds to 2 μm (magnification factor 20000).

XPS of (non-) irradiated MoS₂:

Additional XPS data of non-irradiated and irradiated MoS₂ on Si/SiO₂ substrates are given in Fig. S4. Again, we compared XPS spectra of non-irradiated (Fig. 4 (a)) and irradiated (Fig. S4 (b)) MoS₂ on SiO₂/Si substrates. In analogy to Fig. 5, we witnessed a strong decrease of the S concentration. Comparing the intensity of the S 2p peaks with the Si 2s, we see a clear decrease in the amount of S. While the non-irradiated sample showed an intensity ratio of $I_{S\ 2p}/I_{Si\ 2s} \sim 0.21$, the irradiated one showed a ratio of just 0.13.

Note that for the intensity ratios of Mo/S only relative and no absolute values are calculated, therefore no RSF were taken into consideration.

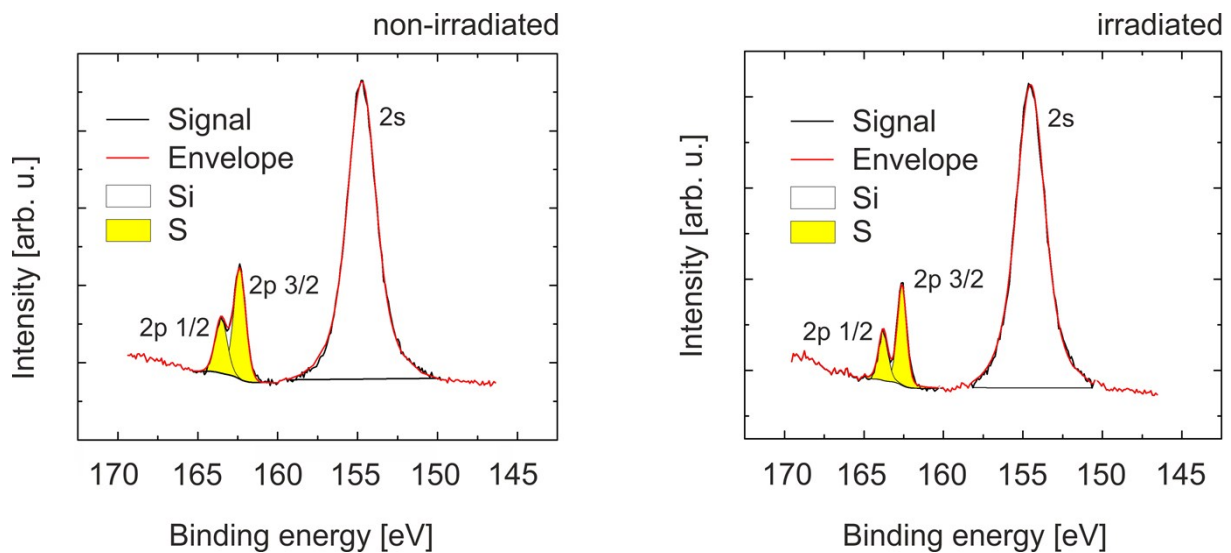


Figure S4: XPS spectra of non-irradiated (a) and irradiated (b) MoS₂ on SiO₂/Si substrates. Comparing the intensity ratios $I_{S\ 2p}/I_{Si\ 2s}$ prior and after irradiation, we observe a strong decrease from ~ 0.22 down to just 0.13. Measurements were performed with a PHI 5000 Versaprobe II under room temperature.

Two Temperature Model and Molecular Dynamics:

We simulate the SHI irradiation with the two-temperature model (TTM) formalism.^{5,6} This model describes the evolution of the electronic and lattice subsystems with two differential equations coupled with an energy exchange term

$$C_e \frac{\partial T_e}{\partial t} = \nabla(K_e \cdot \nabla T_e) - g(T_e - T_l) + A(r,t)$$

$$\text{and } C_l \frac{\partial T_l}{\partial t} = \nabla(K_l \cdot \nabla T_l) + g(T_e - T_l)$$

, where K denotes the thermal conductivity, C the heat capacity, g the electron-phonon coupling, $A(r,t)$ the initial electronic energy distribution and the subscripts l and e refer to the lattice and electronic subsystems, respectively.

For the irradiation effect in MoS₂ we employ in the simulations the following thermodynamical parameters $K_l = 34.5 \text{ Wm}^{-1}\text{K}^{-1}$ ^{7,8}, C_l from Ref. [9], $K_e = D_e \cdot C_e$, obtained as in Ref. [10,11] and $g = C_e / \tau$ with $\tau \sim 0.6 \text{ ps}$.^{12,13} The electronic heat capacity is calculated from the density of states $g(E)$ ¹⁴ as

$$C_e(T_e) = \int_{-\infty}^{\infty} \frac{\partial f(E, \mu, T_e)}{\partial T_e} g(E) E dE$$

Here we use the free electron density of states $g(E)$ calculated with effective masses $m_h = 0.92 m_0$, $m_e = 0.82 m_0$ ¹⁵ and energy gap $E_g = 1.8 \text{ eV}$.¹⁶

$$g_c(E) = \frac{8\pi\sqrt{2}}{h^3} m_e^2 \sqrt{E - E_c}, E \geq E_c$$

$$g_v(E) = \frac{8\pi\sqrt{2}}{h^3} m_h^2 \sqrt{E - E_v}, E \leq E_v$$

We use the CasP software to obtain the initial amount of energy deposited to the electronic subsystem.¹⁷ This method calculates the energy deposited by an ion to every atom based on its impact parameter. In reality, the ions deposit the energy to the electrons locally, producing an electronic cascade, which propagates several nanometers away from the track. In order to model this mechanism, we bin the energy deposited by the ion along the trajectory in 1 nm bins, and then we redistribute the bin energy spatially perpendicular to the ion trajectory using the Waligorski distribution for electron cascades.¹⁸ We use the electronic energy distribution as initial conditions and solve the differential equations in a 2D grid of dimensions 400x400 nm² and element size 1x1 nm². After 1 ps, we take the lattice energy distribution in the center of the grazing impact point and deposit it to the atoms in the MD cell by adding the velocity in a random direction. We apply the Berendsen thermostat on the borders of the cell to account for the energy dissipation on the bulk. The simulations were performed using the REBO potential for MoS₂¹⁹ with the LAMMPS software.²⁰ The chosen potential reproduces accurately the formation energy of the Sulphur and Molybdenum vacancies,²¹ making it suitable for irradiation applications.

To model the increasing temperature of the SiO₂ substrate after ion impact, we employed the TTM. The region, where the temperature rises above the melting temperature of the particular material, undergoes a phase transition which leads to a permanent modification of the surface after cooling. This region typically manifest itself as a rift or track in the case of grazing incidence.²² Comparing the temperature of SiO₂ substrate with the sublimation temperature of MoS₂ and S allows us to make qualitative assumptions whether or whether not the temperature is high enough to evaporate MoS₂

and/or S. For the calculation of the thermal spike in SiO₂ we used the following parameters: $g = 1.2 \times 10^{19} \text{ W/K m}^3$;²³ $K_l = 1.5 \text{ Wm}^{-1}\text{K}^{-1}$, $C_l = 1 \text{ J/g K}$;²⁴ $K_e = D_e \cdot C_e$ were obtained as described in Ref. [23].

Electrochemical analysis:

The catalytic activity of the MoS₂ catalysts for the hydrogen evolution reaction (HER) was measured at room temperature using a conventional three-electrode configuration connected to a potentiostat (SP-240, Bio-Logic). The catalyst sample was employed as the working electrode, a Pt mesh as the counter electrode and an Ag/AgCl wire (in a saturated 3M KCl solution) as the reference electrode. The electrolyte used for the HER was a 0.5 M H₂SO₄ aqueous solution, which was purged with Ar gas (99.999%) for 30 min before the reaction to remove air and other residual gases. Linear sweep voltammetry (LSV) measurements were performed at a scan speed of 5 mV/s. Applied potential values versus Ag/AgCl were referenced to the reversible hydrogen electrode (RHE) by using the expression: $E_{\text{RHE}} = E_{\text{Ag/AgCl}} + 0.0591\text{pH} + E_{\text{Ag/AgCl}}^0$, where $E_{\text{Ag/AgCl}}$ is the experimentally applied potential and $E_{\text{Ag/AgCl}}^0$ the potential difference between the Ag/AgCl electrode and the normal hydrogen electrode (NHE), which is equal to +0.210 V at room temperature. All voltammograms were corrected through iR compensation for addressing the iR drop between the working electrode and the reference electrode by measuring the solution resistance via electrochemical impedance spectroscopy.

For the linear sweep voltammetry measurements, the current density was calculated by dividing the measured catalytic current by the geometrical surface area of MoS₂ on the glassy carbon substrate. The surface area was determined using the Gwyddion software package²⁵ to analyze SEM images of the sample surface. For the analysis a Gaussian filter (pixel averaging) was first applied to homogenize the background and enhance the contrast between the uncovered substrate area and the MoS₂-covered regions. Automatic edge detection (by threshold) followed by subsequent manual refinement were used to precisely mark the MoS₂ regions. The grain property distribution provided the surface ratio of the marked regions to the surrounding background area. In this way the relative coverage was determined for each SEM image. The results obtained from various SEM images were then averaged to provide the overall coverage of the sample.

The electrode geometrical surface area was 240 mm², with a 16-18 % effective MoS₂ surface coverage depending on the sample pre-treatment (16% on the irradiated and 18% on the non-irradiated samples).

The charge transfer resistance, that provides information on the kinetics of the electrochemical reaction, was determined in our study by electrochemical impedance spectroscopy (EIS). Fig. S5 shows the Nyquist plot of our MoS₂ samples and of a bare glassy carbon substrate at -0.25 V vs RHE. The left and right intersection points of the EIS semicircle with the x-axis indicate the value of the solution resistance (ohmic resistance), used to compensate the iR drop, and the sum of the solution resistance and charge transfer resistance (R_{ct}), respectively. By subtracting the latter value from the former, the charge transfer resistance R_{ct} was determined. A smaller value of R_{ct} means faster electric charge transfer between the catalyst and the reactive species. As seen in Fig. S5, the irradiated MoS₂ sample exhibits a lower charge transfer resistance ($R_{\text{ct, irr}} = 3189 \Omega$), thus faster kinetics, compared to the non-irradiated sample ($R_{\text{ct, non-irr}} = 3617 \Omega$).

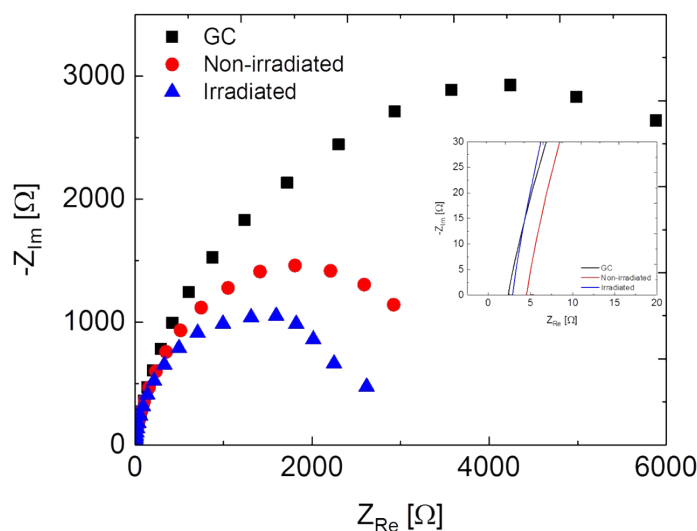


Figure S5. Nyquist plot of irradiated (blue) and non-irradiated (red) MoS₂ samples on glassy carbon, as well as of a bare glassy carbon (GC) substrate (black). The EIS experiments carried out in the frequency range of 1 MHz to 0.1 Hz at -0.25 V vs RHE. The inset shows the high-frequency region of the plot, used for determining the solution resistance.

References

- 1 O. Pollmann, L. Madauß, V. Zeuner and M. Schleberger, *Encyclopedia of Interfacial Chemistry*, *Encyclopedia of Interfacial Chemistry: Surface Science and Electrochemistry*, 2018, **3**, 338–343.
- 2 Z. Liu, M. Amani, S. Najmaei, Q. Xu, X. Zou, W. Zhou, T. Yu, C. Qiu, A. G. Birdwell, F. J. Crowne, R. Vajtai, B. I. Yakobson, Z. Xia, M. Dubey, P. M. Ajayan and J. Lou, Strain and structure heterogeneity in MoS₂ atomic layers grown by chemical vapour deposition, *Nature communications*, 2014, **5**, 5246. DOI: 10.1038/ncomms6246.
- 3 B. Chakraborty, A. Bera, D. V. S. Muthu, S. Bhowmick, U. V. Waghmare and A. K. Sood, Symmetry-dependent phonon renormalization in monolayer MoS₂ transistor, *Phys. Rev. B*, 2012, **85**. DOI: 10.1103/PhysRevB.85.161403.
- 4 H. Guo, Y. Sun, P. Zhai, H. Yao, J. Zeng, S. Zhang, J. Duan, M. Hou, M. Khan and J. Liu, Swift-heavy ion irradiation-induced latent tracks in few- and mono-layer MoS₂, *Appl. Phys. A*, 2016, **122**, 463. DOI: 10.1007/s00339-016-9940-y.
- 5 A. Meftah, F. Brisard, J. M. Costantini, E. Dooryhee, M. Hage-Ali, M. Hervieu, J. P. Stoquert, F. Studer and M. Toulemonde, Track formation in SiO₂ quartz and the thermal-spike mechanism, *Physical Review B*, 1994, **49**, 12457–12463.
- 6 Z. G. Wang, C. Dufour, E. Paumier and M. Toulemonde, The Se sensitivity of metals under swift heavy ion irradiation: a transient thermal process, *Journal of Physics: Condensed Matter*, 1995, **6**, 2525–2526.
- 7 R. Yan, J. R. Simpson, S. Bertolazzi, J. Brivio, M. Watson, X. Wu, A. Kis, T. Luo, A. R. Hight Walker and H. G. Xing, Thermal conductivity of monolayer molybdenum disulfide obtained from temperature-dependent Raman spectroscopy, *ACS nano*, 2014, **8**, 986–993. DOI: 10.1021/nm405826k.
- 8 S. Sahoo, A. P. S. Gaur, M. Ahmadi, M. J.-F. Guinel and R. S. Katiyar, Temperature-Dependent Raman Studies and Thermal Conductivity of Few-Layer MoS₂, *J. Phys. Chem. C*, 2013, **117**, 9042–9047. DOI: 10.1021/jp402509w.
- 9 L. S. Volovik, V. V. Fesenko, A. S. Bolgar, S. V. Drozdova and Klochkov, Primachenko, V. F., Enthalpy and heat capacity of molybdenum disulfide, *Soviet Powder Metallurgy and Metal Ceramics*, 1978, **17**, 697–702.

- 10 C. Dufour, V. Khomenkov, G. Rizza and M. Toulemonde, Ion-matter interaction, *J. Phys. D: Appl. Phys.*, 2012, **45**, 65302. DOI: 10.1088/0022-3727/45/6/065302.
- 11 R. Wang, B. A. Ruzicka, N. Kumar, M. Z. Bellus, H.-Y. Chiu and H. Zhao, Ultrafast and spatially resolved studies of charge carriers in atomically thin molybdenum disulfide, *Phys. Rev. B*, 2012, **86**. DOI: 10.1103/PhysRevB.86.045406.
- 12 Z. Nie, R. Long, L. Sun, C.-C. Huang, J. Zhang, Q. Xiong, D. W. Hewak, Z. Shen, O. V. Prezhdo and Z.-H. Loh, Ultrafast carrier thermalization and cooling dynamics in few-layer MoS₂, *ACS nano*, 2014, **8**, 10931–10940. DOI: 10.1021/nn504760x.
- 13 H. Shi, R. Yan, S. Bertolazzi, J. Brivio, B. Gao, A. Kis, D. Jena, H. G. Xing and L. Huang, Exciton dynamics in suspended monolayer and few-layer MoS₂ 2D crystals, *ACS nano*, 2013, **7**, 1072–1080. DOI: 10.1021/nn303973r.
- 14 Z. Lin, L. V. Zhigilei and V. Celli, Electron-phonon coupling and electron heat capacity of metals under conditions of strong electron-phonon nonequilibrium, *Phys. Rev. B*, 2008, **77**, 776. DOI: 10.1103/PhysRevB.77.075133.
- 15 F. Zahid, L. Liu, Y. Zhu, J. Wang and H. Guo, A generic tight-binding model for monolayer, bilayer and bulk MoS₂, *AIP Advances*, 2013, **3**, 52111. DOI: 10.1063/1.4804936.
- 16 J. Ryou, Y.-S. Kim, S. Kc and K. Cho, Monolayer MoS₂ Bandgap Modulation by Dielectric Environments and Tunable Bandgap Transistors, *Scientific reports*, 2016, **6**, 29184. DOI: 10.1038/srep29184.
- 17 G. Schiwietz and P. L. Grande, Introducing electron capture into the unitary-convolution-approximation energy-loss theory at low velocities, *Phys. Rev. A*, 2011, **84**, 13. DOI: 10.1103/PhysRevA.84.052703.
- 18 M.P.R. Waligórski, R. N. Hamm and R. Katz, The radial distribution of dose around the path of a heavy ion in liquid water, *International Journal of Radiation Applications and Instrumentation. Part D. Nuclear Tracks and Radiation Measurements*, 1986, **11**, 309–319. DOI: 10.1016/1359-0189(86)90057-9.
- 19 T. Liang, S. R. Phillpot and S. B. Sinnott, Parametrization of a reactive many-body potential for Mo–S systems, *Phys. Rev. B*, 2009, **79**, 164. DOI: 10.1103/PhysRevB.79.245110.
- 20 S. Plimpton, Fast Parallel Algorithms for Short-Range Molecular Dynamics, *Journal of Computational Physics*, 1995, **117**, 1–19.
- 21 M. Ghorbani-Asl, S. Kretschmer, D. E. Spearot and A. V. Krasheninnikov, Two-dimensional MoS₂ under ion irradiation, *2D Mater.*, 2017, **4**, 25078. DOI: 10.1088/2053-1583/aa6b17.
- 22 O. Ochedowski, O. Osmani, M. Schade, B. K. Bussmann, B. Ban-d'Etat, H. Lebius and M. Schleberger, Graphitic nanostripes in silicon carbide surfaces created by swift heavy ion irradiation, *Nature communications*, 2014, **5**, 3913. DOI: 10.1038/ncomms4913.
- 23 O. Osmani, N. Medvedev, M. Schleberger and B. Rethfeld, Energy dissipation in dielectrics after swift heavy-ion impact, *Phys. Rev. B*, 2011, **84**, 232. DOI: 10.1103/PhysRevB.84.214105.
- 24 B. El-Kareh, *Fundamentals of Semiconductor Processing Technology*, Springer US, 1st edn., 1995.
- 25 D. Nečas and P. Klapetek, Gwyddion, *Central European Journal of Physics*, 2012, **10**, 181–188. DOI: 10.2478/s11534-011-0096-2.